

Study of the Behavior of Concrete under Triaxial Compression

Domingo Sfer¹; Ignacio Carol, M.ASCE²; Ravindra Gettu³; and Guillermo Etse⁴

Abstract: An experimental study of the confined compression behavior of concrete has been performed using 150×300 mm cylindrical specimens subjected to hydrostatic pressure in a triaxial cell and axial loading through a servo-hydraulic testing machine. A confining stress range of 0 to 60 MPa (about twice the uniaxial compressive strength) was employed to obtain the brittle-ductile transition behavior of the material. The increase in confining pressure leads to a change in the mode of failure and an increase in the maximum axial load-carrying capacity. It is seen that, at zero or low confinement, there is distributed microcracking and several macrocracks, and the response exhibits a well-defined peak and subsequent softening. At high confinements, relatively large axial and transversal strains of over 10% have been obtained, with monotonically increasing loads leading to horizontal plateaus. There is no distributed cracking and failure occurs with the propagation of few macrocracks. In general, the observed trends confirm and extend previous results reported in the literature. Optical microscopy shows extensive microcracking, especially in the aggregates, and pore collapse at high confinement. A preliminary interpretation of the results based on the theory of elastoplasticity is also presented.

DOI: 10.1061/(ASCE)0733-9399(2002)128:2(156)

CE Database keywords: Triaxial compression; Concrete; Fractures; Elastoplasticity.

Introduction

The behavior of concrete under high levels of confinement is of significant importance in several engineering problems, such as the design of the anchorage of prestressing reinforcement, containment vessels, bridge piles and columns of high rise buildings and impact of projectiles. Since the pioneering work of Balmer (1949), many researchers have studied the confined behavior of concrete, especially over the last three decades (Kotsovos and Newman 1978; Newman 1979; van Mier 1986; Wang et al. 1987; Smith et al. 1989; Bellotti and Rossi 1991; Chern et al. 1992; Dahl 1992; Imran and Pantazopoulou 1996; Li and Ansari 1999). Generally, cylindrical specimens were loaded axially while subjecting them to constant lateral pressure in a triaxial cell. In most cases, cylinders with diameters of 100 mm or less have been used. Though the reported confining pressures are normally not higher than the uniaxial compressive strength (f_c) of the concrete, some researchers have used pressures of up to $5f_c$.

The testing of concrete under triaxial stresses can provide valuable information, not only for design purposes but also for the development and validation of constitutive models. The first step

in such modeling could be the application of the flow theory of elastoplasticity, which has traditionally been used in soil mechanics and geotechnical engineering, and appears to be well suited for simulating the “ductile” behavior of confined concrete (Smith et al. 1989). Moreover, many of its concepts (e.g., loading surfaces, flow rules for inelastic strains) are present in more recent approaches that have been formulated to simulate the brittle behavior of concrete, such as in continuum damage mechanics (Li and Ansari 1999; Carol et al. 2001). Also, in order to provide the necessary data for modeling, an appropriate theoretical framework should be considered in the design of experiments, as in the work of Smith et al. (1989), which has largely motivated the present study.

This paper describes the results of an ongoing study of the triaxial behavior of concrete, as well as some interpretations of the results based on elastoplasticity. The noteworthy features of the test program include the use of a conventional specimen, a 150×300 mm molded cylinder, which is larger than those used in most other studies; the measurement of axial strains up to 10%; the use of a wide range of confining pressures up to $2f_c$; and the determination of a significant part of the postpeak response.

Materials and Specimens Used

The concrete used in the experimental study was designed to have a characteristic compressive strength of 30 MPa at 28 days, and had the proportions of cement:sand:gravel:water = 1:2.5:2.8:0.57, by weight. The materials used were cement of type CEM I 42.5R, crushed limestone sand (size range of 0–5 mm, fineness modulus=3.1), crushed limestone gravel of two size ranges (5–12 mm and 12–20 mm, in the ratio of 1:6, by weight), and a modified lignosulfonate plasticizer (dosage = 0.4 L/m³, density = 1.18 kg/L, 40% solid content).

The concrete was fabricated in a 250 L forced-action mixer. The slump of the fresh concrete, measured with the standard

¹Civil Engineering Dept., Univ. Nacional de Tucumán, Avda. Independencia 1800, 4000 Tucumán, Argentina.

²Univ. Politècnica de Catalunya, ETSECCPB, Jordi Girona 1-3, 08034 Barcelona, Spain.

³Univ. Politècnica de Catalunya, ETSECCPB, Jordi Girona 1-3, 08034 Barcelona, Spain.

⁴Civil Engineering Dept., Univ. Nacional de Tucumán, Avda. Independencia 1800, 4000 Tucumán, Argentina.

Note. Associate Editor: Arup K. Maji. Discussion open until July 1, 2002. Separate discussions must be submitted for individual papers. To extend the closing date by one month, a written request must be filed with the ASCE Managing Editor. The manuscript for this paper was submitted for review and possible publication on November 17, 2000; approved on April 9, 2001. This paper is part of the *Journal of Engineering Mechanics*, Vol. 128, No. 2, February 1, 2002. ©ASCE, ISSN 0733-9399/2002/2-156-163/\$8.00+\$5.00 per page.

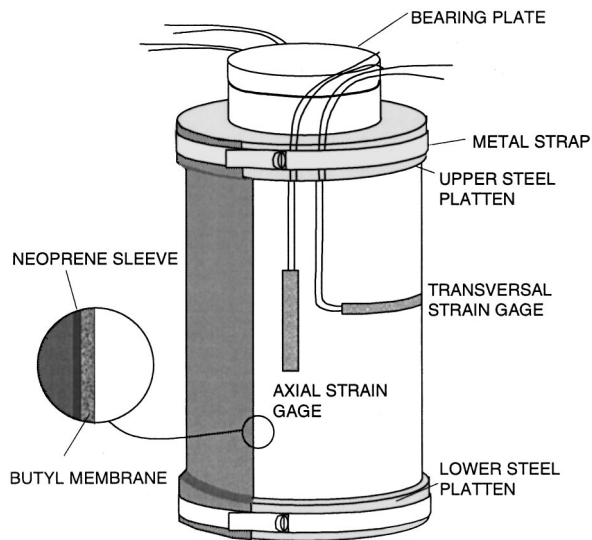


Fig. 1. Specimen prepared for triaxial testing

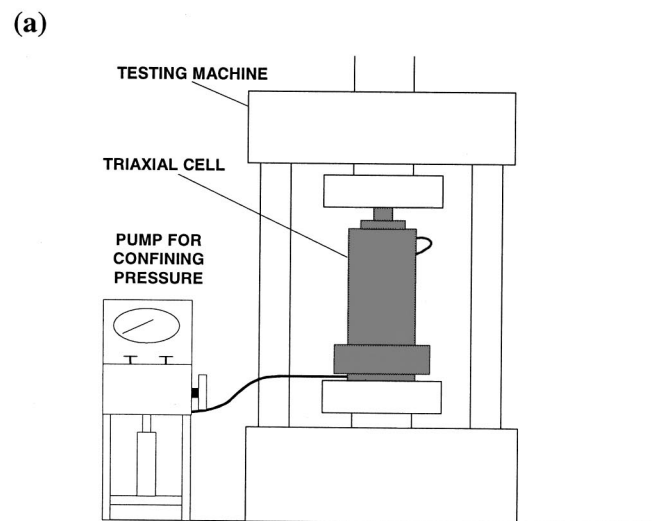
Abrams cone, was 15 cm. As mentioned earlier, standard cylindrical specimens (of 150 mm diameter and 300 mm height) were cast in metal molds. The specimens were demolded after 24 h and stored in a fog room until testing.

Experimental Details

The specimens for the triaxial tests were prepared as shown in Fig. 1. A 3-mm-thick butyl sleeve was placed around the cylinder and an impermeable neoprene sleeve was fitted over it. Previously, the larger surface voids were filled with cement mortar, which along with the butyl layer reduces the possibility of the neoprene sleeve being punctured during the test. Also, before placing the sleeves, two pairs of strain gages (60-mm-long, strain capacity greater than 10%) were glued on the surface of the specimen at midheight. One pair was located along the axial direction and the other perpendicular to it, with the gages situated diametrically opposite to each other. Steel loading plattens were placed at the flat ends of the specimen and the sleeves were tightened over them with metal straps to avoid the ingress of oil. In order to minimize the friction at the contact, 0.1-mm-thick Teflon sheets were placed between the loading plattens and the specimen (cf. van Mier et al. 1997), in addition to polishing the specimen ends with a diamond disk. A spherical bearing plate was placed on top of the upper loading platten for the application of the axial load. Note that the loading plattens had to be slightly larger than 150 mm in diameter since the specimens undergo significant transversal expansion during the tests.

The tests were performed in the configuration shown schematically in Fig. 2(a), using a servohydraulic testing machine, with a compressive load capacity of 4.5 MN, and a Wykeham Farrance triaxial cell, with a pressure capacity of 140 MPa. The cell consists of a steel chamber with a rigid pedestal base [see Fig. 2(b)]. The axial load from the testing machine is transmitted to the specimen by a piston that passes through the top of the cell. The cell is filled with castor oil and a known hydrostatic pressure is applied with a pump.

During the tests, the hydrostatic pressure, axial load (measured with a ΔP cell), surface strains and the displacement of the piston of the cell [measured with a 25-mm span linear variable differen-



(a)

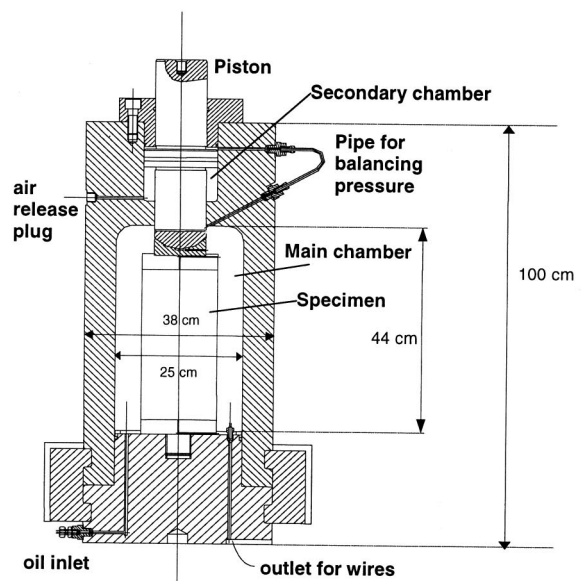


Fig. 2. (a) Test setup and (b) cross section of the triaxial cell

tial transformer (LVDT)] were monitored at a frequency of 1 reading/s using a PC-based data acquisition system and LabTech Notebook software.

The objective of mounting gages on the specimen surface was to determine the axial and transversal strains. However, the strain gages do not yield reliable measurements beyond the peak load (due to cracking and strain localization). Therefore, in the post-peak regime, the piston displacement was divided by the original specimen height to obtain an average nominal axial strain. Comparing the prepeak responses given by the strain gages and the LVDT, and subtracting the differences from the entire LVDT measurements as a function of the load, a correction for the effect of the end conditions is obtained.

Several levels of confining pressure (σ_L) were used in order to study the brittle-ductile transition of the response: 1.5, 4.5, 9.0, 30.0, and 60.0 MPa, which correspond to approximate σ_L/f_c ratios of 0.00, 0.05, 0.15, 0.30, 1.00, and 2.00, respectively. First, the prescribed hydrostatic pressure was applied in the cell, and then the axial load was increased at a constant piston-displacement rate of 0.006 mm/s. The tests were terminated at an

Table 1. Failure Modes under Different Lateral Pressures

σ_L (MPa)	Specimen 1		Specimen 2	
0.0				
1.5				
4.5				
9.0				
30.0				
60.0				

axial strain of 10% or at an axial postpeak load equal to 10% of the peak load. After each test, the specimen was removed from the cell and the surface crack patterns were recorded. It was later cut with a saw to observe the mode of failure. Two specimens were tested at each confining pressure, and all tests were performed at ages of more than 50 days to minimize the effect of aging on the response. In addition to the triaxial tests, uniaxial compression tests (without confining pressure) were also performed.

Results and Discussion

Table 1 shows the observed failure modes as a function of the confining pressure, using photographs and idealized crack pat-

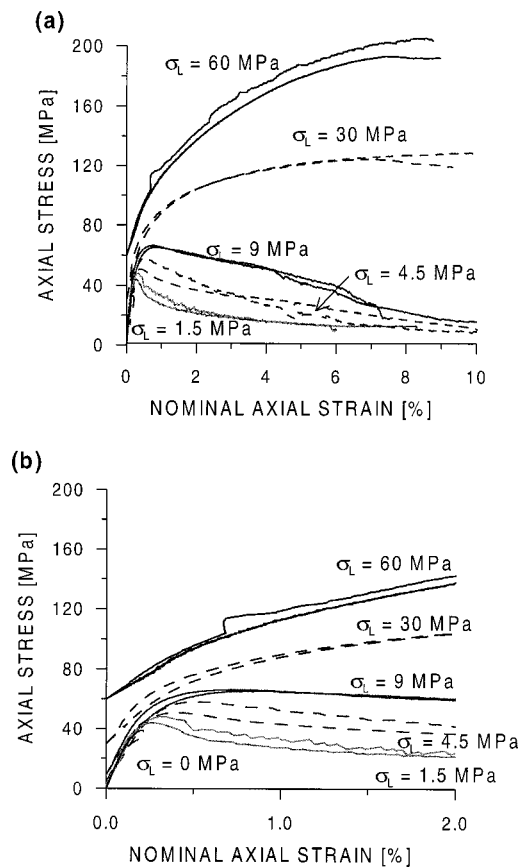


Fig. 3. Axial stress-strain response for different confining stresses, (a) complete curves and (b) enlargement of the initial part of the curves

terns after completion of the test. It can be seen that, at low confining pressures ($\sigma_L < 4.5$ MPa), the failure occurs with the propagation of several distributed vertical and inclined cracks. On the other hand, at higher confining pressures ($\sigma_L > 4.5$ MPa), the specimen breaks suddenly in an unsymmetric manner into just two or three pieces, as also seen in recent tests of Rutland and Wang (1997).

The axial stress-strain responses of the specimens at different confining pressures are represented in Fig. 3(a). For each level of confinement, two curves are shown corresponding to each of the specimens tested. Note that the axial stress takes into account the initial hydrostatic pressure, and therefore, the curves do not begin from zero but from the value of the confining pressure. As mentioned earlier, the nominal axial strain is obtained from the piston displacement, after correcting the values with those obtained from the strain gages in the prepeak regime. The curves in Fig. 3(b) give the initial response of the specimens, at low strains, where a decrease in the initial slope of the curve is observed with an increase in confining pressure.

The load-carrying capacity of the concrete, at a given axial strain, increases significantly, as expected, with an increase in confining pressure. Up to the confining pressure of 9 MPa (i.e., approximately $0.3f_c$), the curves exhibit well-defined peak loads and smoothly descending post-peak curves. The peak load increases and the steepness of the post-peak response decreases with an increase in the confining pressure, indicating an increase in the effective compressive strength and the ductility with confinement. The response in the low confinement regime is compat-

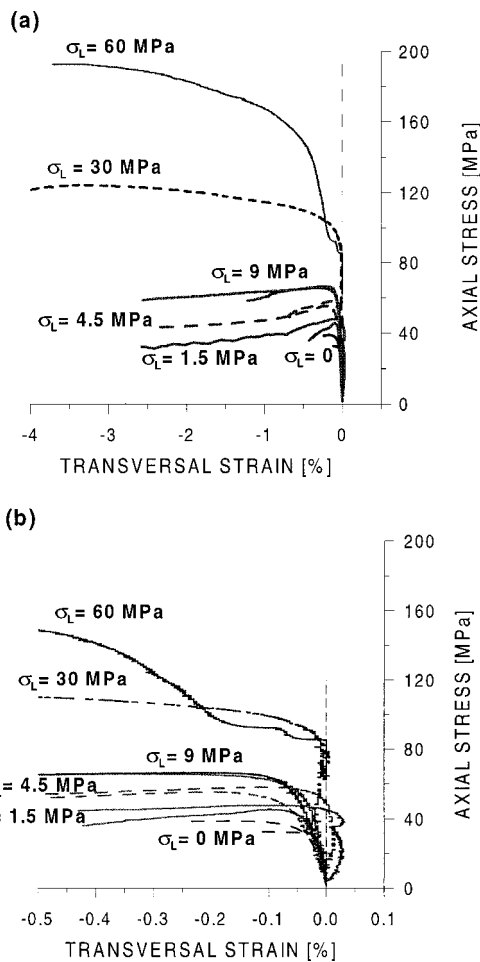


Fig. 4. Axial stress-versus transversal strain response for different confining stresses, (a) complete curves and (b) enlargement of the initial part of the curves

ible with the observed failure modes, where extensive micro-cracking and several macrocracks are seen at failure.

At the higher levels of confinement, at 30 and 60 MPa (i.e., about 100 and 200% of f_c), the response does not exhibit a well-defined peak but a monotonically decreasing slope tending toward a plateau. This apparently ductile behavior and increased mechanical integrity at large strains is in accordance with the presence of just one or two macrocracks without any distributed cracking, as observed after the test. The consequent friction between the separated blocks contributes significantly to the post-peak load-carrying capacity. The abrupt termination of the plateau can be attributed to the sudden propagation of these macrocracks, and the possible loss of confinement due to the ingress of oil.

In Figs. 4(a and b), the transversal strain is represented against the axial stress for all the specimens tested, except for one specimen at each of the pressures of 30 and 60 MPa, in which it was not properly registered. Here and later on, positive strains denote a reduction in the dimensions or contraction.

The transversal and axial strains may be summed to obtain the volumetric strain, which is represented in Fig. 5 as a function of the axial stress. In this figure, it is apparent that, after the initial contraction (i.e., volume reduction), the trend is reversed just before the peak when the material starts exhibiting dilatancy (i.e., volume increase). It appears that this change in trend (i.e., dilatancy) occurs much earlier than the maximum load for higher confining stresses.

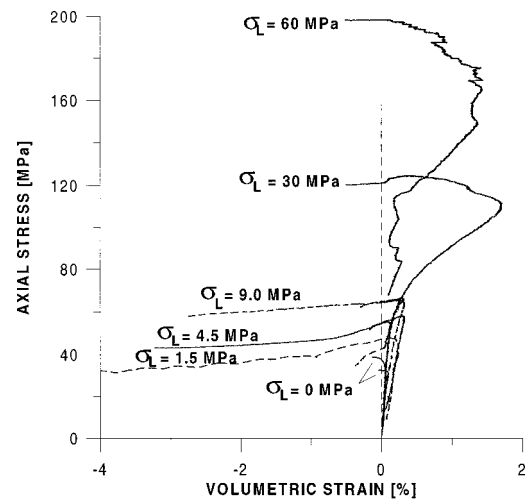


Fig. 5. Volumetric strain versus axial stress, for different confining stresses.

In Table 2, the mean maximum axial stress or confined compressive strength (σ_{peak}) for each σ_L is given, along with other representative results. Note that the σ_L/f_c ratios have been calculated with the f_c -value obtained at approximately the same age as that corresponding to the triaxial test. The axial strains at the peak, ϵ_{peak} , and the initial slope of the axial stress-strain curves (at the beginning of the application of the axial load), E_0^{tan} , are also given in Table 2. Note that the latter is not the modulus of elasticity, except in the case of $\sigma_L=0$. The data show the almost sixfold increase in the maximum load due to the highest level of confinement (60 MPa) and the increase in the peak strain by about two orders of magnitude. The progressive decrease in the initial slope is in accordance with the results of previous researchers, such as Dahl (1992).

The increasing confined compressive strengths are depicted graphically in Fig. 6, along with the data of Li and Ansari (1999). In order to compare the experimental values with those predicted by existing failure envelopes, the curves obtained with the following models of Richart et al. and Newman and the extended Leon model (Etse and Willam 1994) are also represented in the same figure.

Table 2. Test Results

σ_L (MPa)	age (days)	σ_L/f_c (%)	σ_{peak} (MPa)	ϵ_{peak} (%)	E_0^{tan} (GPa)
0.0	51	0	32.8	0.18	27.3
	114	0	38.8	0.21	28.6
1.5	64	4.6	45.5	0.26	26.1
	114	3.9	47.8	0.34	22.5
4.5	69	13.7	55.3	0.41	22.4
	112	11.6	58.2	0.52	17.7
9.0	59	27.4	65.7	0.83	15.5
	108	23.2	66.5	0.63	18.9
30.0	56	91.5	124.5	7.0	13.4
	85	77.3	129.3	10.9	10.1
60.0	51	182.9	192.9	8.5	7.1
	106	154.6	205.1	8.3	7.9

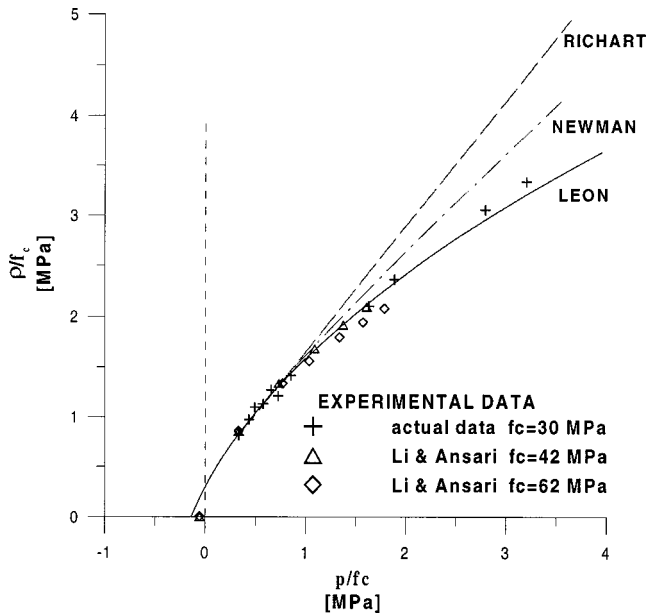


Fig. 6. Comparison of experimental results with existing failure envelopes

Richart et al. (1928):

$$f_c + 4.1\sigma_L - \sigma_3 = 0 \quad (1)$$

Newman (1979):

$$\sqrt{A \left(\frac{\sigma_L}{f_c} \right)^2 + B \frac{\sigma_L}{f_c} + 1} - \frac{\sigma_3}{f_c} = 0 \quad (2)$$

where A and B are empirical parameters

Etse and Willam (1994):

$$\frac{3}{2} \frac{\rho^2}{f_c^2} + \frac{m}{f_c} \left[-p + \frac{\rho}{\sqrt{6}} \right] = 0 \quad (3)$$

where

$$m = \frac{f_c^2 - f_t^2}{f_c f_t}$$

In the above equations, compression is considered as positive, $p = \text{mean stress} = I_1/3$; $\rho = \text{octahedral shear stress} = \sqrt{2J_2}$; $I_1 = \text{first invariant of stress} = \sigma_1 + \sigma_2 + \sigma_3$; $J_2 = \text{second invariant of deviatoric stress} = \frac{1}{6}[(\sigma_1 - \sigma_2)^2 + (\sigma_1 - \sigma_3)^2 + (\sigma_2 - \sigma_3)^2]$; $f_t = \text{uniaxial tensile strength}$; and $\sigma_1, \sigma_2, \sigma_3 = \text{principal stresses ordered as } \sigma_1 \leq \sigma_2 \leq \sigma_3$ (in these tests $\sigma_1 = \sigma_2 = \sigma_L < \sigma_3$).

The experimental data in Fig. 6 show similar trends as the data by Li and Ansari (1999), even though the concrete strengths were substantially higher. They also compare relatively well with the predictions of the extended Leon model, while the other two expressions seem to represent only the behavior at lower confinement well. A recent model of Kang (1997) gave the same predictions as that of extended Leon model.

In order to evaluate the internal state of the concrete subjected to high confinement, prisms of $50 \times 50 \times 80$ mm were cut from one of the specimens tested at the confining pressure of 60 MPa. Visual inspection of the surfaces indicated good mechanical integrity of the concrete, without any pulverized material. The prisms were subjected to uniaxial compression and it was found that the concrete previously subjected to a strain of over 10% retained about 40% of the strength observed in identical speci-

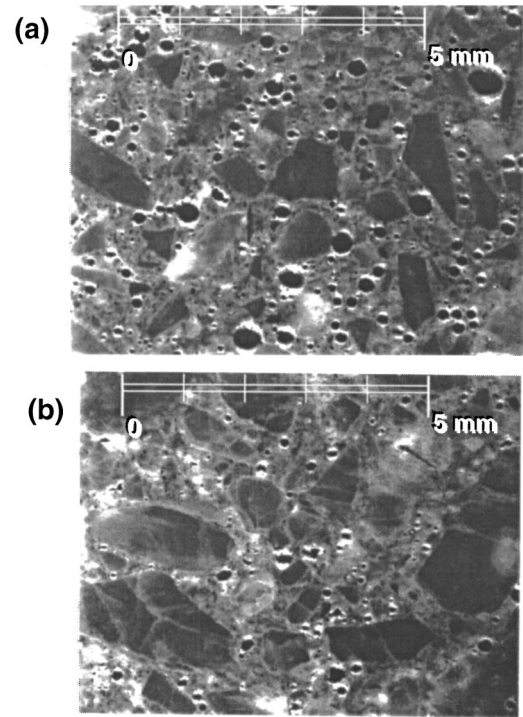


Fig. 7. Optical micrographs of thin sections of (a) virgin concrete and (b) concrete subjected to 60 MPa confining pressure

mens cut from virgin concrete and about 50% of the modulus of elasticity. Such behavior has often been, at least partially, attributed to the compaction of the concrete under confinement. This was further studied by making thin section slides of the concrete subjected to 60 MPa lateral pressure and of the virgin concrete, and analyzing them with optical microscopy. The corresponding micrographs are shown in Figs. 7(a and b), respectively. It is obvious that the pores (seen as black spots) seen in the virgin concrete are far more numerous and larger in size than those seen in the previously tested concrete, which implies significant alterations in the internal structure due to the large strains under confinement. This is also that the compaction occurs with the pore collapse in the paste and extensive distributed microcracking in the aggregates.

The effect of the compaction was further studied through an additional triaxial test on a similar concrete with $\sigma_L = 40$ MPa, where unloading-reloading cycles were performed during the application of the axial load in order to estimate the change in the stiffness during the loading, as shown in Fig. 8. It is observed that the unloading-reloading stiffness, which is clearly much higher than the initial tangent stiffness, decreases very little over the range of applied axial strain (up to 8%), probably due to the closure of the microcracks under high confinement. These aspects are in agreement with the conclusions of other researchers (Smith et al. 1989, Imran et al. 1996).

Interpretation of Results in the Framework of Elastoplasticity

Elastoplasticity is a well-established theory that, in addition to encompassing several aspects of the behavior of concrete under high confinement, leads to the rational interpretation of experimental observations (Smith et al. 1989). The basic concepts and

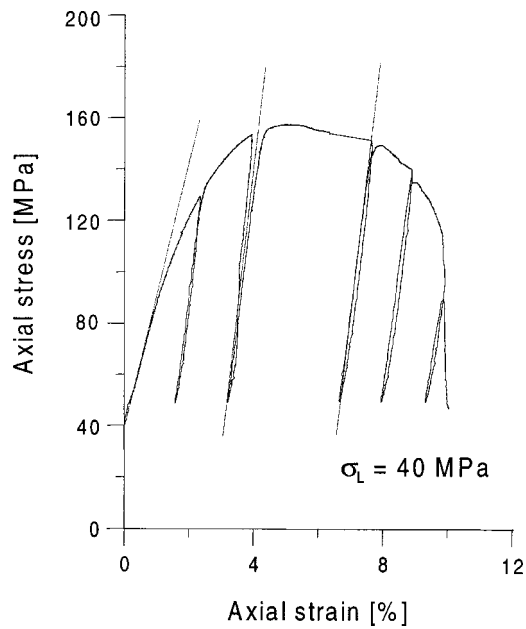


Fig. 8. Unloading-reloading curves under constant lateral pressure

equations used in this section are summarized in the Appendix, and more general descriptions can be found in textbooks such as that of Chen (1982).

As seen earlier, compaction under confined compression seems to be an important aspect of the behavior due to which the initial slope of the load-displacement curve decreases with an increase in lateral pressure [Fig. 3(b)]. On the other hand, it has been mentioned that the unloading-reloading stiffness is higher and does not degrade with an increase in the axial strain, even at relatively large values of up to 8–10% (Fig. 8). Such behavior can be explained in the context of elastoplasticity by considering a loading surface with a “cap,” which limits the elastic region along the direction of hydrostatic pressure or the p axis (see Fig. 9). In such a model, high hydrostatic pressure takes the stress state to the cap of the yield surface, after which plastic strains develop from the very beginning of the deviatoric loading. Consequently, the initial slope of the axial stress-strain curves de-

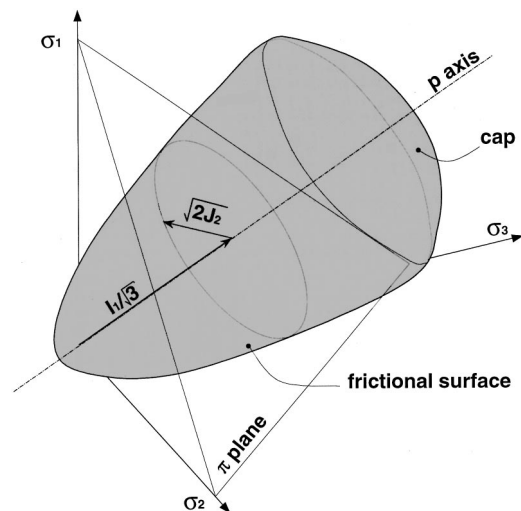


Fig. 9. Loading surface with “cap” in principal stress space

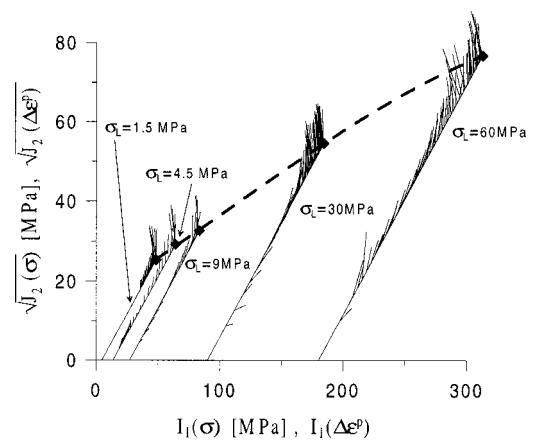


Fig. 10. Experimental failure envelope and plastic strain vectors in $I_1, \sqrt{J_2}$ space

creases with an increase in the hydrostatic pressure, corresponding to the evolution of the elastoplastic stiffness.

Although the formulation of a complete constitutive model for confined concrete is beyond the scope of the present paper, a preliminary basis can be developed using the experimental results obtained here, in terms of the shape of the yield function and trends of the flow rule. This can be done considering the biaxial space defined by invariants I_1 and $\sqrt{J_2}$, which corresponds to a cross section of the general yield surface of Fig. 9, along a plane containing the p axis. Consequently (see the Appendix), the experimental results take the form shown in Fig. 10. In this diagram, every possible stress state in the material is represented by one point, although different stress states may lead to the same I_1 and J_2 , and therefore be given by the same point. The evolution of stresses corresponding to each of the triaxial tests performed in this study is then represented by a horizontal line from the origin to the given confining pressure, followed by an inclined line that corresponds to the application of the axial load. The stress trajectory for each test ends at a point that corresponds to the peak load. All such points have been joined to get the dashed line in the diagram that gives the approximate shape of the loading surface of a model in the $I_1 - \sqrt{J_2}$ space.

In the same diagram (Fig. 10), the short-thin lines represent the direction of the increments of plastic strain at different stages of the loading history, given by the strain variables dual to I_1 and $\sqrt{J_2}$ (i.e., volumetric strain and the square root of J_2 of the plastic strain increment; see the Appendix for more details). Each of these lines starts from the corresponding stress and indicates the experimentally obtained direction of the plastic flow rule. Note that, in this representation, a horizontal segment indicates a purely volumetric strain increment, with expansion to the left of the stress path and contraction to the right, while a vertical segment indicates a purely deviatoric strain increment (i.e., constant volume). Although affected by the scatter intrinsic to the test data, a clear tendency is observed for the plastic volumetric components that start mainly as contractions (i.e., lines to the right of the stress path), later vanish, and finally become dilatant (i.e., lines to the left of the stress path). It can also be clearly seen that the plastic strains at the peak are not necessarily normal to the surface, confirming the results reported in the literature (e.g., Smith et al. 1989) indicating that concrete indeed exhibits nonassociative behavior.

Within the framework of elastoplasticity and continuum mechanics, the termination of the plateau behavior at high confine-

ment levels can also be explained in a natural manner. The sudden drop in axial stress physically corresponds to the propagation of one or two macrocracks through the specimen. The onset of these cracks may be treated as the emergence of discontinuities in a medium with initially continuous stress and strain, similar to the case of the initiation of shear bands in soils (Rudnicki 1975; Ortiz 1987; Rizzi et al. 1995). Such instability analysis, based on the singularity condition of the so-called “acoustic” or “localization” tensor, requires the availability of an appropriate (normally elastoplastic) constitutive model and may often be performed analytically (Runesson et al. 1991). A preliminary analysis of this type applied to the present test data has been carried out (Etse et al. 2001) using the extended Leon model for the constitutive behavior. The results indicate that the uniaxial compressive loading would not lead to localization before or near the peak, unless the imperfections in the geometry and/or loading intervene. The randomness of the imperfections could explain the inconsistent crack patterns observed in Table 1 for higher confinement, as discussed earlier.

Conclusions

Experimental results obtained from confined compression tests of concrete, using cylindrical specimens of 150×300 mm, have been reported. The responses observed are qualitatively and quantitatively similar to those of previous experimental studies, most of which used smaller test specimens. The maximum load-carrying capacity under axial compression increases significantly with an increase in the confining pressure. At low confinement, the response exhibits a well-defined peak followed by a smoothly descending curve, while at higher confinement, the response is ductile, with a monotonically increasing load leading to a plateau.

The increase in confining pressure leads to a change in the principal failure mechanism: instead of distributed cracking there is fine microcracking and few macrocracks that separate the specimen into two or three blocks. Optical micrographs of the internal structure of the concrete before and after the triaxial tests indicate considerable distributed microcracking within the aggregates, and the collapse of pores in the compaction process leading to significantly large strains, up to 10%, before failure occurs with the propagation of a few macrocracks.

Elastoplasticity offers a convenient framework for interpreting the results obtained in the tests, explaining, for example, the decrease in the slope of stress strain curves at the beginning of the deviatoric loading. Analysis of the experimental data leads to a basis for the shape of the loading surface and the main aspects of the flow rule to be used in elastoplastic models for concrete.

Acknowledgments

Partial funding for this study was provided by the DGES-MEC (Madrid, Spain) Research Grant Nos. PB95-0500, PB98-0928, and MAT2000-1007 to the UPC. The stay of the first writer in Barcelona was made possible by Grants No. FOME C 044 from UNT (Tucumán, Argentina) and No. 1997SGR00048, from the Generalitat de Catalunya (Barcelona, Spain). The tests reported here were performed at the Structural Technology Laboratory of the UPC. The writer wish to thank Professor Stein Sture for his stimulating comments and for sharing with them the extensive experience on triaxial testing at the Univ. of Colorado, Boulder. The help of C. Bernad and S. Valls during the experimental study is gratefully appreciated.

Appendix: Basic Equations of Elastoplasticity

Considering the standard decomposition of strain in the plastic regime:

$$\Delta \varepsilon = \Delta \varepsilon^e + \Delta \varepsilon^p \quad (4)$$

The elastic strains are always related to the increments and total values of stresses through linear isotropic elasticity; that is, in Cartesian components and index notation:

$$\varepsilon_{ij}^e = -\frac{\nu}{E} \sigma_{kk} \delta_{ij} + \frac{1+\nu}{E} \sigma_{ij} \quad (5)$$

or, with the principal components:

$$\varepsilon_1^e = \frac{1}{E} \sigma_1 - \frac{\nu}{E} (\sigma_2 + \sigma_3) \quad (6a)$$

$$\varepsilon_2^e = \frac{1}{E} \sigma_2 - \frac{\nu}{E} (\sigma_3 + \sigma_1) \quad (6b)$$

$$\varepsilon_3^e = \frac{1}{E} \sigma_3 - \frac{\nu}{E} (\sigma_2 + \sigma_1) \quad (6c)$$

Using the experimentally obtained values of strain and stress, the plastic strain may be regarded simply as the difference between the measured total strain and the elastic strains corresponding to the applied stresses. In other words, the plastic strain is considered as the strain exceeding that predicted by linear elasticity.

Considering the lateral pressure in the triaxial cell, σ_L , and the total axial stress σ_1 as the stress variables, for a small load increment during the test, we have $\Delta \sigma_2 = \Delta \sigma_3 = 0$, the stress increment $\Delta \sigma_1$, and the strain increments $\Delta \varepsilon_2 = \Delta \varepsilon_3 = \Delta \varepsilon_L$. For this load increment, we can combine Eqs. (5) and (6) and substitute to obtain:

$$\Delta \varepsilon_1^p = \Delta \varepsilon_1 - \frac{1}{E} \Delta \sigma_1 \quad (7a)$$

$$\Delta \varepsilon_2^p = \Delta \varepsilon_3^p = \Delta \varepsilon_L - \frac{\nu}{E} \Delta \sigma_1 \quad (7b)$$

Considering the axes defined by the invariants $I_1(\sigma)$ and $\sqrt{J_2(\sigma)}$ (which may be directly interpreted as a cut through the yield surface in Fig. 9 along a plane containing the p axis), the plastic strain increments may be represented by the conjugate quantities $I_1(\Delta \varepsilon^p)$ and $J_2(\Delta \varepsilon^p)$.

Substituting the values obtained previously in the invariant expressions, we get the four quantities represented in Fig. 10:

$$I_1(\sigma) = \sigma_1 + 2\sigma_L \quad (8a)$$

$$I_1(\Delta \varepsilon^p) = \Delta \varepsilon_1 + 2\Delta \varepsilon_L - \frac{1-2\nu}{E} \Delta \sigma_1 \quad (8b)$$

$$\sqrt{J_2(\sigma)} = \frac{1}{\sqrt{3}} |\sigma_1 - \sigma_L| \quad (8c)$$

$$\sqrt{J_2(\Delta \varepsilon^p)} = \frac{1}{\sqrt{3}} \left| \Delta \varepsilon_1 + 2\Delta \varepsilon_L - \frac{1-2\nu}{E} \Delta \sigma_1 \right| \quad (8d)$$

Notation

The following symbols are used in this paper:

E_0^{tan} = initial tangent modulus;

f_c = uniaxial compressive strength of concrete;
 I_1 = first invariant of stress;
 J_2 = second invariant of deviatoric stress;
 p = mean stress ($I_1/3$);
 $\Delta \varepsilon_1, \Delta \varepsilon_2, \Delta \varepsilon_3$ = increments of principal strain components;
 $\Delta \sigma_1, \Delta \sigma_2, \Delta \sigma_3$ = increments of principal stress components;
 δ_{ij} = Kronecker delta components;
 ε_{ij} = strain tensor components;
 ε_{ij}^e = elastic strain tensor components;
 $\varepsilon_{\text{peak}}$ = axial strain at peak;
 $\varepsilon_1^p, \varepsilon_2^p, \varepsilon_3^p$ = principal plastic strain components;
 $\varepsilon_1^e, \varepsilon_2^e, \varepsilon_3^e$ = principal elastic strain components;
 $\varepsilon_1, \varepsilon_2, \varepsilon_3$ = principal strains components;
 ν = Poisson's ratio;
 σ_{ij} = stress tensor components;
 σ_L = confinement; lateral stress;
 $\sigma_1, \sigma_2, \sigma_3$ = principal stress components; and
 σ_{peak} = axial stress at peak.

References

- Balmer, G. G. (1949). "Shearing strength of concrete under high triaxial stress-Computation of Mohr's envelope as a curve." *Tech. Rep. No. SP-23*, Structure Research Laboratory, Denver.
- Bellotti, R., and Rossi, P. (1991). "Cylinder tests: Experimental technique and results." *Mater. Struct.*, 24, 45–51.
- Carol, I., Rizzi, E., and Willam, K. (2001). "On the formulation of anisotropic elastic degradation. I Theory based on a pseudo-logarithmic damage tensor rate." and "II Generalised pseudo rankine model for tensile damage." *Int. J. Solids Struct.*, 38(4), 491–546.
- Chen, W. F. (1982). *Plasticity in reinforced concrete*, McGraw-Hill, New York.
- Chern, J.-C., Yang, H.-J., and Chen, H.-W. (1992). "Behavior of steel fiber reinforced concrete in multiaxial loading." *ACI Mater. J.*, 89, 32–40.
- Dahl, K. K. B. (1992). "A failure criterion for normal and high strength concrete." *Rep. R. 286*, Department of Structural Engineering, Technical Univ. of Denmark, Lyngby, Denmark.
- Etse, G., and Willam, K. (1994). "Fracture energy formulation for inelastic behavior of plain concrete." *J. Eng. Mech.*, 120(9), 1983–2011.
- Etse, G., Sfer, D., Carol, I., Gettu, R., and Willam, K. (2001). "Dilatational response of concrete materials: Facts and fiction." *ACI Special Publication*, American Concrete Institute, in press.
- Imran, I., and Pantazopoulou, S. J. (1996). "Experimental study of plain concrete under triaxial stresses." *ACI Mater. J.*, 93, 589–601.
- Kang, H. D. (1997). "Triaxial constitutive model for plain and reinforced concrete behavior." PhD thesis, Univ. of Colorado, Boulder, Colo.
- Kotsovos, M. D., and Newman, J. B. (1978). "Generalized stress-strain relations for concrete." *J. Eng. Mech.*, 104(4), 845–856.
- Li, Q., and Ansari, F. (1999). "Mechanics of damage and constitutive relationships for high-strength concrete in triaxial compression." *J. Eng. Mech.*, 125(1), 1–10.
- Newman, J. B. (1979). "Concrete under complex stresses." *Development in concrete technology-1*, F. D. Lydon, ed., Applied Science, London.
- Ortiz, M. (1987). "An analytical study of the localized failure modes of concrete." *Mech. Mater.*, 6, 159–174.
- Richart, F. E., Brandtzaeg, A., and Brown, R. L. (1928). "A study of the failure of concrete under combined compressive stresses." *Engineering Experiment Bulletin No. 185*, Univ. of Illinois, Urbana, Ill.
- Rizzi, E., Carol, I., and Willam, K. (1995). "Localization analysis of elastic degradation with application to scalar damage." *J. Eng. Mech.*, 121(4), 541–554.
- Runesson, K., Ottosen, N. S., and Peric, D. (1991). "Discontinuous bifurcation of elasto-plastic solutions in plane stress and plane strain." *Int. J. Plast.*, 7, 99–121.
- Rudnicki, J. W., and Rice, J. R. (1975). "Conditions for the localization of deformation in pressure-sensitive dilatant materials." *J. Mech. Phys. Solids*, 23, 371–394.
- Rutland, C. A., and Wang, M. L. (1997). "The effects of confinement of the failure orientation in cementitious materials: Experimental observations." *Cem. Concr. Composites*, 19, 149–160.
- Smith, S. S., Willam, K. J., Gerstle, K. H., and Sture, S. (1989). "Concrete over the top, or is there life after the peak?" *ACI Mater. J.*, 86, 491–497.
- van Mier, J. G. M. (1986). "Fracture of concrete under complex stresses." *Heron*, 31(3), 1–89.
- van Mier, J. G. M., et al. (1997). "Strain-softening of concrete in uniaxial compression." *Mater. Struct.*, 30, 195–209.
- Wang, C.-Z., Guo, Z.-H., and Zhang, X.-Q. (1987). "Experimental investigation of biaxial and triaxial compressive concrete strength." *ACI Mater. J.*, 84, 92–100.